NOTES AND CORRESPONDENCE

Atmospheric Effects on Upper-Ocean Temperature in the Southeast Tasman Sea

M. G. HADFIELD

National Institute of Water and Atmospheric Research, Ltd., Wellington, New Zealand

23 November 1999 and 23 May 2000

ABSTRACT

The temperature profile in the ocean mixed layer was simulated using a turbulence closure model for a period of 18 years (1980–97) at a site in the southeast Tasman Sea (42°S, 170°E). The simulation was forced at the surface by a meteorological dataset derived from land station data. Sea surface temperature (SST) from the model was compared with the NCEP 1° SST analysis, beginning in 1982. The mean annual cycle and monthly anomalies in modeled SST agree with the NCEP dataset in several respects. Modeled and observed SST anomalies are highly correlated with each other and are similar in overall magnitude, timescale, and phase. However, the model underpredicts the magnitude of SST anomalies in winter. Modeled and observed SST lagged-correlation fields are similar, with both showing a high correlation of SST anomalies in winter with anomalies in the previous spring. The model has a pronounced recurrence mechanism; that is, anomalous temperatures in the deep mixed layer in spring remain below the shallower summer mixed layer and reappear at the surface in the following autumn and winter. Model experiments involving artificial atmospheric perturbations and/or damping of subsurface anomalies both indicate that subsurface storage alone does not account for the spring–winter correlation and that atmospheric cooperation is required.

1. Introduction

Hadfield and Sharples (1996) modeled SST, mixed layer depth, nutrients, and phytoplankton biomass at a site (42°S, 170°E) in the southeast Tasman Sea. Their model gave a good hindcast of SST and mixed layer depth; it agreed with the limited nutrient data with respect to the time of the arrival of significant nitrate concentrations at the surface in late autumn or early winter. (This is a sensitive test of the medel's handling the erosion of the seasonal thermocline.) The present note uses a similar model and presents a more systematic comparison of model results with SST observations.

The model is forced by surface heat and momentum fluxes that are calculated from an 18-yr synthetic meteorological dataset based on land station observations. The ocean mixed layer is represented on a multilevel grid using a turbulence closure scheme. The ocean below the mixed layer is highly simplified and essentially passive; horizontal and vertical advection are ignored. Surface fluxes are computed using the model's simulated SST. As noted in previous studies (e.g., Frankignoul 1985, p. 371), this constrains the model SST not to depart markedly from observed SST because of the feedback of SST on air temperature and the high correlation between the two variables. The importance of this constraint for the present study is considered in the discussion.

Section 2 describes the site. Section 3 describes the model. Section 4 compares modeled SST with observed SST, finding generally good agreement. There are several interesting aspects of the SST monthly anomaly statistics that point to importance of the breakdown in the seasonal thermocline in autumn bringing deeper water to the surface and thereby affecting winter SST. In section 5 the persistence of SST anomalies under the summer mixed layer is quantified and manipulated artificially to investigate its importance. The results are discussed in section 6.

2. The site

The site is one where a model neglecting horizontal advection should have a reasonable chance of working. It is in subtropical water, 120 km west of South Island, New Zealand (Fig. 1) and several hundred kilometers away from major ocean fronts (Heath 1981, 1985; Stanton and Ridgway 1988). The mean current is weak (<0.1 m s^{-1}) and fluctuating currents are dominated by coastal trapped waves propagating southward along the South Island west coast (Cahill et al. 1991; Stanton and

Corresponding author address: Dr. Mark Hadfield, National Institute of Water and Atmospheric Research, Ltd., PO Box 14-901, Wellington, New Zealand.
E-mail: m.hadfield@niwa.cri.nz

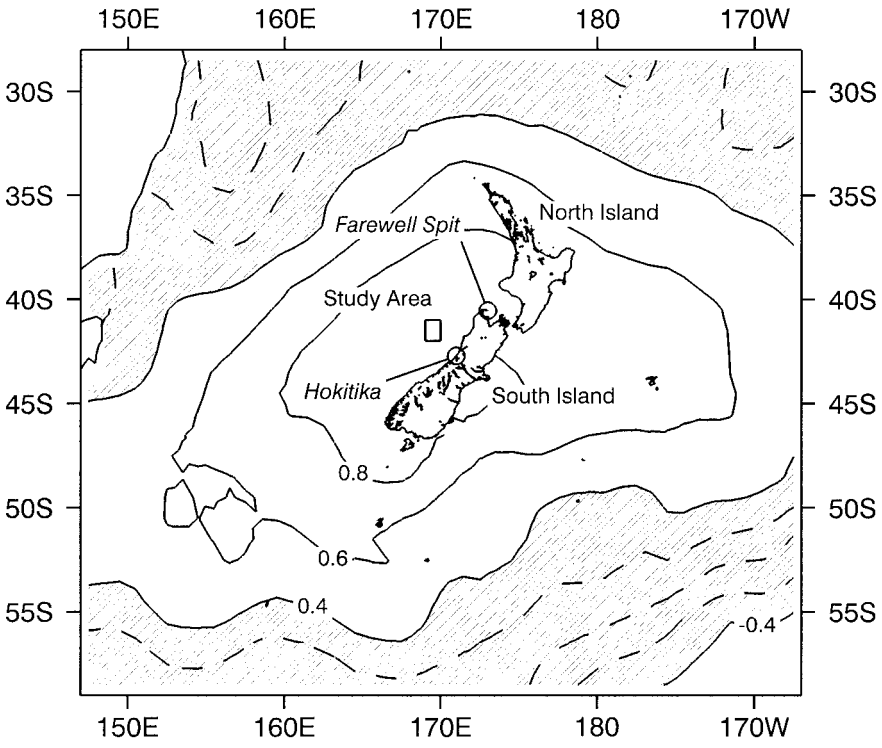

FIG. 1. Map showing the study area and the meteorological stations, with contours of the correlation between monthly SST anomalies at each location and anomalies at the study area. SST data are from the NCEP dataset.

Greig 1991). No systematic analysis of back trajectories is available, but water in the area has probably entered the Tasman Sea either via the East Australia Current or around Tasmania and crossed the Tasman Sea over several months (Hamilton 1992; Mullan 1998). From the National Centers for Environmental Prediction (NCEP) SST analysis (Reynolds and Smith 1994) the mean SST gradient is directed to the northeast and has magnitude 0.35°C per 100 km, which is lower than the average in the Tasman Sea. Within 50 km or so of the South Island coast, there is frequently a shallow mixed layer (a few tens of meters deep) throughout the year resulting from river outflow, but signs of this are seldom observed at the study area (Heath and Ridgway 1985; Moore and Murdoch 1993; Stanton 1976; Stanton and Moore 1992).

Weather at the site is dominated throughout the year by an irregular succession of eastward-moving cyclones and anticyclones. The mean wind speed is 7 m s^{-1}. The net heat flux has an annual amplitude of 140 W m^{-2} and a mean within ± 10 W m^{-2} (Hadfield and Sharples 1996, Fig. 6). Monthly anomalies in net heat flux have a standard deviation of 25 W m^{-2}. There is little seasonal variation in the wind speed or the heat flux variability. These estimates are based on the current model, but are supported by our analysis of surface fluxes from the NCEP/NCAR Reanalysis dataset (Kalnay et al. 1996).

Figure 1 also shows contours of the correlation coefficient between monthly SST anomalies at each point in the domain with SST anomalies at the study area. This indicates the large spatial scale of SST anomalies, as has been noted previously (Frankignoul 1985). The correlation exceeds 0.60 over a belt up to 20° in latitude, extending westward into the southern Tasman Sea and eastward of central New Zealand. This suggests that the results are not just locally applicable.

3. The model

a. Model formulation

The model is similar to that described by Hadfield and Sharples (1996). It has prognostic equations for temperature, salinity, and horizontal velocity. Horizontal velocity is included only to allow a shear production term in the turbulence budget. There is a fixed vertical grid with a cell thickness of 4 m at the surface and a uniform stretch factor of 1.055; there are 40 cells in total and the lower boundary is at 546 m. Vertical diffusion is paremeterized with the Gaspar et al. (1990) turbulence closure scheme (see also Bougeault and Lacarrere 1989), which has a prognostic equation for turbulence kinetic energy (TKE) and a diagnostic equation for turbulence length scale. Although this model has a novel length scale formulation, it behaves very similarly

to other turbulence closure models in mixed layer simulations (Ayotte et al. 1996; Large et al. 1994). The present scheme departs from Gaspar et al. (1990) in that it includes a surface TKE flux of $10(\tau/\rho_w)^{3/2}$ to represent mechanical stirring by surface waves, where τ is the surface stress and ρ_w is the density of water (Noh 1996); this has an effect only when the mixed layer is very shallow.

Hadfield and Sharples (1996) found it necessary to constrain profiles of temperature, salinity, and velocity below the mixed layer by imposing relaxation toward a prescribed base state. Since the current work is concerned with persistence over timescales of the order of 1 year, the effect of this process on persistence of subsurface anomalies was of concern. In the simulations described below the relaxation coefficient γ is equal to 0.5 a^{-1} at 200-m depth and below; above that it drops linearly to zero at the surface. Variations in the coefficient by a factor of 2 either side of this value were found to have very little effect on the results. Reducing γ to zero allows the temperature near the bottom of the domain to rise steadily, owing to a small downward heat flux supported by the background diffusivity in the turbulence scheme.

Salinity must be included in the model for satisfactory treatment of the permanent pycnocline, where the density gradient due to salinity is equal to -0.57 times the density gradient due to temperature. Hadfield and Sharples included a surface salinity budget with rainfall and evaporation terms, but here surface salinity is simply nudged toward a fixed value with a timescale of 30 days.

Fluxes of momentum, heat, and TKE at the ocean surface are calculated via conventional bulk parameterizations. The exchange coefficients for momentum, sensible heat, and latent heat (C_D, C_T, and C_E) are evaluated via the iterative scheme of Smith (1988). The resulting coefficients are functions of wind speed and atmospheric surface layer stability. In neutral conditions, C_D is close to 1.0×10^{-3} for wind speeds up to 5 m s^{-1} then increase approximately linearly with wind speed, C_T is independent of wind speed at 1.0×10^{-3}, and $C_E = 1.2C_T$. Of the shortwave radiative flux, 5% is reflected at the surface, 76% is absorbed in the top grid cell, and the remainder is distributed down the water column with an absorption coefficient 0.055 m^{-1}. There is a simple daily cycle in solar input, with a seasonally varying day length. (This degree of sophistication is unnecessary for the present work but relevant for simulations that resolve the diurnal cycle in turbulence.) Net longwave radiation is calculated with the formula of Berliand and Berliand (1952) with the Hastenrath and Lamb (1978) cloud correction factor—see Fung et al. (1984).

Numerical implementation is straightforward, via forward-in-time, centered-in-space finite differences. The time step was calculated at each iteration to stay within the numerical stability constraint for diffusion, and was limited to a maximum of 180 s.

b. Meteorological data

The meteorological dataset is described by Hadfield and Sharples (1996) and in more detail by Hadfield (1995). Wind data was taken from Farewell Spit (40°33.0′S, 173°01.2′E), an exposed coastal site at the northwest tip of South Island (Fig. 1). Temperature, humidity, and insolation data were taken from Hokitika (42°43.2′S, 170°59.4′E), on the coast near the study area. The meteorological data were adjusted to apply over the sea via simple additive or multiplicative corrections derived from comparisons of at-sea meteorological data with the land station data. At sea data were taken from routine synoptic reports (most of them from research vessels) and a meteorological buoy deployed at 42°47.1′S, 170°05.9′E from 1995 (Stanton 1998). For the present work, there were a few changes from Hadfield (1995). Daily average dry bulb and wet bulb temperatures over the sea T_d and T_w were estimated from 3-hourly observations at Hokitika with the formulas

$$T_d = (T_{D09} + T_{D12} + T_{D15} + T_{D18})/4 + C_{d0} + C_{d1}\sin(2\pi[t - t_0]/\tau) + C_{d2}\cos(2\pi[t - t_0]/\tau) \quad (1)$$

$$T_w = (T_{W09} + T_{W12} + T_{W15} + T_{W18})/4 + C_{w0} + C_{w1}\sin(2\pi[t - t_0]/\tau) + C_{w2}\cos(2\pi[t - t_0]/\tau), \quad (2)$$

where T_{D09}, T_{W09}, etc. are Hokitika dry bulb temperatures during the daylight hours (0900, 1200, 1500, and 1800 local time), t is time in days, t_0 is 0000 on 1 January 1980, τ is one year, and the parameters of the seasonally varying land–sea correction are $C_{d0} = 0.51$°C, $C_{d1} = 0.33$°C, $C_{d2} = 1.37$°C, $C_{w0} = 0.65$°C, $C_{w1} = 0.75$°C, $C_{w2} = 1.18$°C. Insolation is taken from daily Hokitika insolation measurements, adjusted for the small latitude difference. Cloud cover (used only in the longwave calculations) is estimated from the ratio between Hokitika daily insolation and a clear-sky value. Wind speed is taken from Farewell Spit 3-hourly measurements multiplied by 1.2 (Hadfield and Sharples 1996; Rahmstorf 1992), with a further factor of 1.35 applied before August 1985 to compensate for a site change. For wind direction, Farewell Spit measurements are used unaltered—this ignores major topographic effects on wind flow around South Island, but wind direction is not important for the mixed layer model in any case, as long as the pattern of variability is not grossly unrealistic.

The base state profiles for temperature and salinity were

$$T_b(z) = 14.65\text{°C} - (0.0113\text{°C m}^{-1})z \quad (3)$$

$$S_b(z) = 35.4 - (0.0015\ \text{m}^{-1})z. \quad (4)$$

These profiles were derived from piecewise linear fits to observed profiles below the mixed layer. The base

state velocity $\mathbf{u}_b$ was set to zero to suppress long-term drift in the velocity below the mixed layer. Temperature, salinity, and velocity were initialized with their base state profiles.

4. Comparison with observations

a. Mean annual cycle

Model SST was compared with SST from the NCEP dataset at 41.5°S, 169.5°E. The weekly NCEP data were smoothed temporally with a 1–2–1 filter as recommended by R. W. Reynolds (1995, personal communication) and the model SSTs were filtered with a 7-day running mean and interpolated to the same times as the NCEP analysis. The mean difference (model minus observations) is −0.14°C and the standard deviation is 0.70°C.

The model temperatures were averaged over each calendar month, then averages and anomalies for each month were calculated for the 16 years from 1982 to 1997. NCEP SST data at 41.5°S, 169.5°E were processed in the same way. The mean values for each month are compared in the upper panel of Fig. 2. The model SST has a similar seasonal range to the NCEP SST, but lags by 1 month. The largest differences occur in December–January (model SST 0.9°C cooler) and April–May (model 0.7°C warmer). In the lower two panels of Fig. 2 the model subsurface temperature is compared with monthly profiles at 41.5°S, 169.5°E from the *World Ocean Atlas 1994* (Levitus et al. 1994); our unpublished evaluation of the ocean atlas in the New Zealand region shows that temperatures are typically within 0.5°C of other sources (the ocean atlas SST being on average approximately 0.2°C warmer than the NCEP SST) but there are scattered erroneous values, usually quite conspicuous in relation to surrounding data. The thick lines on the contour plots represent the mixed layer depth, defined here as the depth at which the mean temperature for each month drops to 0.5°C below the surface value. Again, agreement is good. The model forms a seasonal thermocline at the right depth (approximately 40 m) and the modeled maximum mixed layer depth (260 m) is a little larger than in the ocean atlas (230 m). However, stratification of the model mixed layer in spring lags by about 1 month, which is consistent with the model SST being too cool at this time of year. Note also that the temperature gradient in the model's seasonal thermocline is more sharply defined than in the ocean atlas data, and the temperature gradient between depth 100 and 200 m is correspondingly weaker.

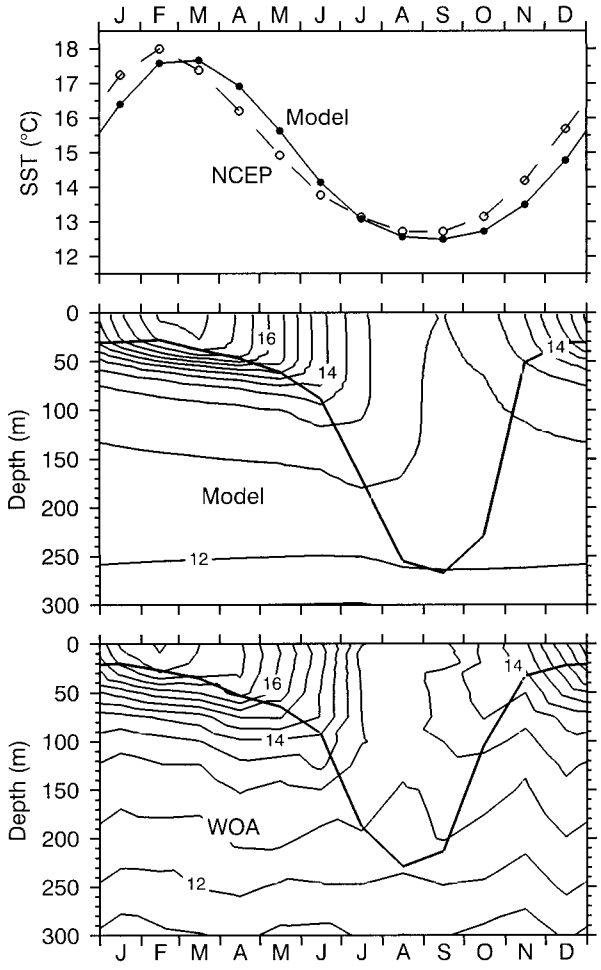

FIG. 2. Mean annual cycle in modeled and observed temperature. All graphs share the same horizontal axis, representing time of year in months. The upper panel shows SST for the model and NCEP datasets. The other two panels show contours of subsurface temperature for the model (center) and the *World Ocean Atlas 1994* (lower) datasets. The solid line shows the depth at which the temperature drops to 0.5°C below the surface temperature.

b. Monthly anomalies

Figure 3 shows time series of model monthly anomalies in SST and vertically integrated temperature, along with NCEP monthly SST anomalies. The model and NCEP SST anomaly series appear to correspond very closely in magnitude and phase, the most obvious discrepancies being that an observed negative anomaly in early 1987 is not reproduced by the model and that the large negative anomaly observed in summer 1982/83 is somewhat too large in the model. The overall correlation is 0.83 and correlation coefficients for individual months vary between 0.74 in July and 0.91 for February (Table 1). The vertically integrated temperature anomaly (hereafter called the heat anomaly) is computed over the entire model domain but, because the model temperature at depth is relaxed toward climatology, it effectively represents the anomaly in heat storage down to the maximum depth of the winter mixed layer. Model heat anomalies are highly correlated with SST anomalies in late winter and early spring, the maximum correlation coefficient being 0.95 in September and October (Table 2). The heat anomaly graph in Fig. 3 is dominated by

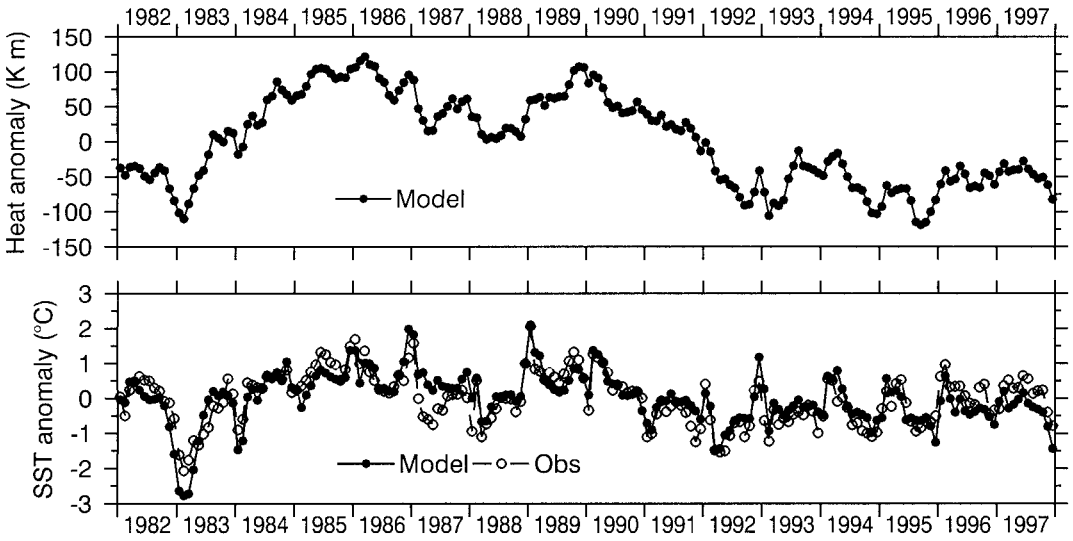

FIG. 3. Time series of model and NCEP monthly SST anomalies (lower panel) and model vertically integrated temperature anomalies (upper panel).

a slow variation between negative in the early 1980s, positive during the middle and late 1980s, and negative throughout the 1990s.

The seasonal variation in the standard deviation of SST and heat anomalies is shown in Fig. 4. In the NCEP data, the standard deviation varies by a factor of more than 2, between 0.5° (Aug) and 1.1°C (Jan). The corresponding variation in the model SST is even more pronounced: the standard deviation is slightly larger than the observations in summer and 30% smaller than the observations in winter. It drops sharply between April and June and rises sharply between October and December. Figure 4 also shows the standard deviation of the model heat anomaly. This quantity has very little seasonal variation, which suggests that the smaller SST variability in winter results from the larger thermal inertia of the mixed layer at that time of year.

Lagged autocorrelations of the SST anomalies are shown in Fig. 5. For each month of the year, m, and lag, l, the contour graphs show the correlation $r_{m,l}$ of the monthly temperature anomaly series T'_m, T'_{m+12}, . . . , $T'_{m+12(n-1)}$ with T'_{m+l}, T'_{m+12+l}, . . . , $T'_{m+12(n-1)+l}$, where $n = 16$ is the number of years. The contour graphs are shaded in the range ± 0.6, outside which individual correlation values are nonzero with 95% confidence. (This is only an approximate estimate of the confidence in the results because it is calculated from the standard error for a single $r_{m,l}$ value and it has been assumed that all the years are independent.) The upper plot shows the average of $r_{m,l}$ over all months m; it is equal to the autocorrelation of the anomaly series where they have been normalized by the mean standard deviation for each month.

There are several noteworthy features in Fig. 5. The rate at which the autocorrelation drops away from unity at small lags is a measure of short-term decorrelation; the lag-1 autocorrelation $r_{m,1}$ can be related to a timescale $\tau_m = -1/\ln r_{m,1}$ for each month. The value of τ based on the averaged autocorrelations (central graph) is similar for both datasets, namely 5 months. The NCEP SST autocorrelation has a clearly defined seasonal cycle, with $\tau \sim 2.5$ months in summer and $\tau \sim 12$ months for the rest of the year. In the model, τ in summer is a little larger than for the NCEP anomalies, at around 3.5 months, and there is a conspicuous break in persistence around June: SST anomalies in July are much more highly correlated with anomalies in the following months (e.g., $r_{7,2} = 0.81$) than are SST anomalies in May (e.g., $r_{5,2} = 0.64$). This feature is less pronounced, but not absent, in the observed SST anomaly correlations ($r_{7,2} = 0.77$, $r_{5,2} = 0.86$).

Another conspicuous feature in the averaged autocorrelations (Fig. 5 upper panel) is a broad peak at 9–12 months lag in both the modeled and NCEP datasets. In the seasonally stratified autocorrelations (lower panels), both datasets show a secondary maximum at around 9 months lag for base months in spring. In the NCEP dataset the largest correlation occurs between each November and the following August ($r_{11,9} = 0.70$). In the model SST there is a broader peak, at 7–12 months lag,

TABLE 1. Correlation between simulated and observed SST anomalies by month and overall.

Jan	Feb	Mar	Apr	May	Jun	Jul	Aug	Sep	Oct	Nov	Dec	Overall
0.89	0.91	0.84	0.81	0.84	0.75	0.74	0.84	0.84	0.83	0.83	0.86	0.83

TABLE 2. Correlation between model SST and heat anomalies by month.

Jan	Feb	Mar	Apr	May	Jun	Jul	Aug	Sep	Oct	Nov	Dec
0.66	0.56	0.62	0.62	0.72	0.86	0.92	0.94	0.95	0.95	0.90	0.78

involving correlations of SST in late winter/spring with SST in the subsequent winter; the largest correlation occurs between November and the following June ($r_{11,7} = 0.81$). This appears to be an example of the recurrence pattern noted in North Pacific SST data by Namias and Born (1970, 1974) and analyzed using surface and subsurface data from four ocean weather station (OWS) sites in the North Pacific and North Atlantic by Alexander and Deser (1995). The hypothesis is that temperature anomalies in late winter/early spring are stored beneath the surface in summer and reentrained into the mixed layer in the following fall and winter. The maximum spring–winter SST correlation observed at this site, $r = 0.7$, is large compared to the values found by Alexander and Deser [$r \sim 0.6$ at OWS C (52°45′N, 35°30′W) and $r < 0.4$ at the other three sites]. The mechanism by which this spring–winter correlation is maintained will be explored further in section 5.

c. Other evidence

Several other analyses have been done to assess the accuracy of the model's SST hindcast and the response of the model to atmospheric forcing. They will not be reported in detail here. Seasonally stratified, lag correlations between model and NCEP SST anomalies, similar to the single-variable lagged correlations presented in Fig. 5, show that the model SST anomalies are in phase with the observed anomalies to within 1–2 months. The model's sensitivity to changes in the meteorological data was assessed by imposing perturbations with various magnitudes and temporal patterns. It was found that air temperature is the most important variable controlling SST, and that the timescale of the mixed layer response to a perturbation varies strongly with season.

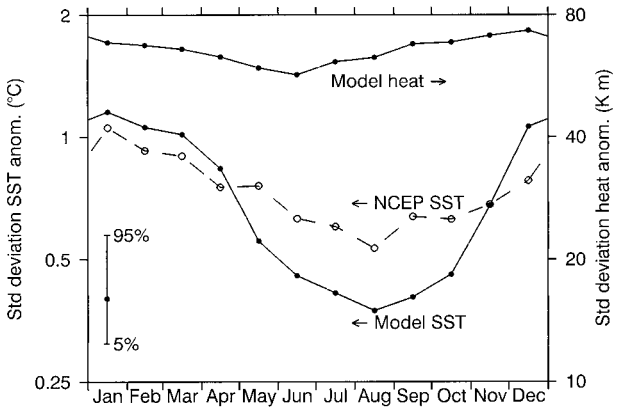

FIG. 4. Standard deviation of model monthly SST anomalies, observed SST anomalies and model heat anomalies, vs time of year. The vertical bar represents confidence intervals for each standard deviation estimate, assuming $N - 1$ degrees of freedom, where $N = 16$ is the number of years; this range is the same for all values on the logarithmic vertical axis.

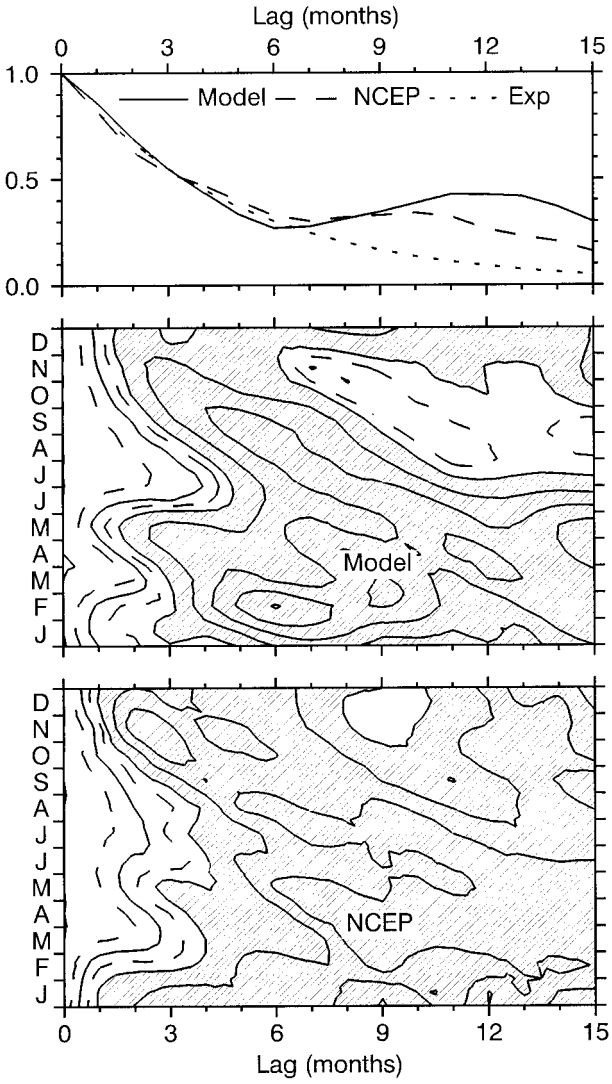

FIG. 5. Lagged SST anomaly autocorrelations by month. All graphs share the same horizontal axis, representing lag in months. The upper panel shows the autocorrelation averaged over the year for model (solid) and NCEP (long dashes), along with an exponential curve, $\exp(-\lambda \text{ lag})$, (short dashes) with timescale $\lambda^{-1} = 5$ months. The other two panels show contours of the autocorrelation vs time of year for the model (center) and NCEP (bottom) anomalies. The vertical axis shows the base month from Jan to Dec (upward). Contours are at intervals of 0.2 (solid) and also at 0.7 and 0.9 (dashed); the hatched region represents values below 0.6.

It has been noted by many authors (e.g., Frankignoul 1985, p. 371) that, in a model which calculates SST using observed air temperature, the model SST is constrained to agree with the observed one because of the feedback of SST on air temperature and the good correlation between the two variables. Thus, at the suggestion of a reviewer, the model was subjected to a more stringent test where surface heat fluxes were calculated using observed SST instead of modeled SST. To prevent drift a negative feedback term was added to the heat flux, as follows:

$$Q_r = a_r(T_m - T_o), \tag{5}$$

where T_m and T_o are modeled and observed SST, respectively, and a_r is equal to 20 W m^{-2} K^{-1} (Frankignoul et al. 1998). It was found that this formulation does lead to a reduction in the accuracy of the model. Mean SST in spring and early summer (which the model already underpredicts) is reduced by approx. 0.3°C; the overall correlation between modeled and observed monthly SST anomalies is reduced from 0.83 to 0.71. The spring–winter recurrence effect remains significant but the maximum correlation is reduced slightly (e.g., $r_{11,7} = 0.75$).

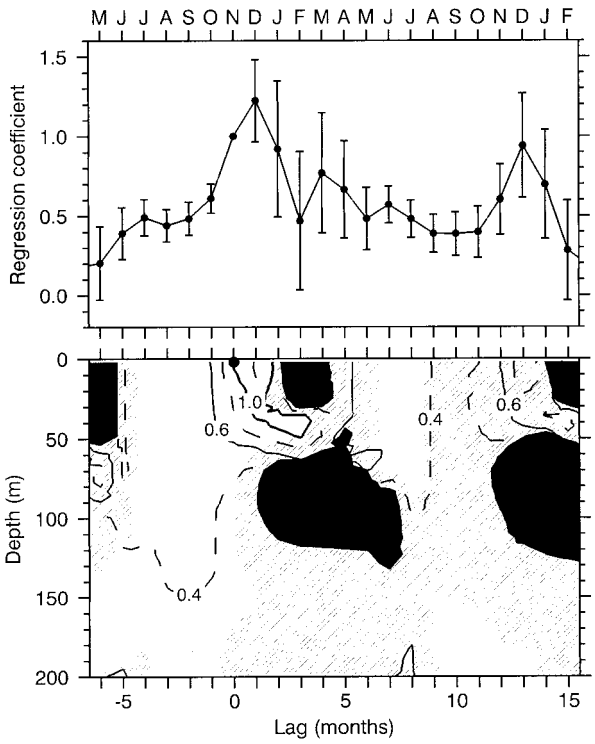

FIG. 6. Coefficients for linear regression between the model SST in Nov (independent variable) and lagged anomalies in model SST and subsurface temperature. The upper panel shows the SST coefficients with bars to ±1 standard error. The lower panel shows contours of the subsurface temperature coefficients with shading depending on the squared correlation coefficient: black indicates $r^2 < 0.25$, hatched indicates $0.25 < r^2 < 0.50$, and unshaded indicates r^2 0.50.

5. Heat storage below the summer mixed layer

a. Defining the temperature anomaly pattern

To explore the spring–winter recurrence pattern noted in connection with Fig. 5, linear regression coefficients were calculated for various combinations of the SST anomaly in a base month in spring (independent variable) with SST and other anomalies at a range of lags. Results are presented here for a base month of November because that is the month showing the largest lagged correlations. The regression analysis addresses questions of the form: Given a certain SST anomaly in November, what is the best estimate (and associated uncertainty) of the anomaly *n* months later in quantity *x*? Figure 6 shows the slope coefficients for SST and subsurface temperature regressed against November SST. For SST (upper panel) the estimated slope coefficients at 7–10 months lag (in Jun–Sep following the base month) are between 0.4 and 0.55, with standard error 0.2 or less. Coefficients over the intervening summer and autumn are generally positive, but with larger standard error. At one month lag the slope coefficient for the model (but not the NCEP dataset) is larger than unity, by one standard error, suggesting that the SST anomalies in November tend to amplify over the following month, possibly because the associated meteorological anomalies persist. There is also a prominent peak one year later, suggesting a year-to-year persistence in the meteorological anomalies. The subsurface signature (lower panel) associated with November SST anomalies can be seen in the form of a lobe of coefficients near unity descending to 40-m depth (i.e., near the top of the seasonal thermocline) in February. This is similar to the patterns seen in OWS data and mixed layer simulations by Alexander and Deser (1995), and is consistent with the mechanism proposed for the SST recurrence pattern. November SST is also highly correlated with surface and subsurface anomalies up to four months previously, which is not surprising given the generally high persistence of SST anomalies from winter into spring (Fig. 5); thus the recurrence of SST anomalies from spring to the following winter is connected (in the model) to a general year to year persistence of temperature anomalies below the seasonal thermocline.

The finding that SST anomalies in spring persist below the mixed layer over summer is consistent with previous work, but the extent to which these anomalies reappear at the surface in autumn, as measured by the spring–winter SST correlation, varies among midlatitude sites (Alexander and Deser 1995). In the present data the spring–winter SST correlation is high (as large as 0.7 in the observed data and 0.8 in the model). The importance of the model's subsurface heat storage in generating the high correlation was assessed by two artificial manipulations.

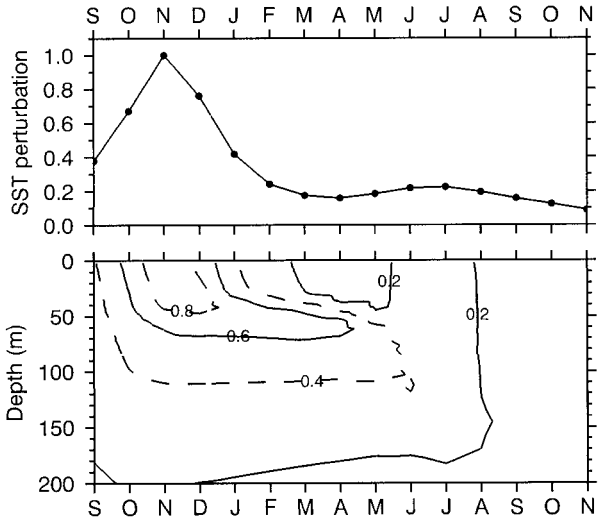

FIG. 7. Monthly averaged temperature perturbation calculated for a set of simulations in which the air temperature was perturbed for four months ending 30 Nov (see text). Monthly averages are normalized by the mean perturbation in Nov. The upper panel shows surface temperature and the lower panel shows contours of the subsurface temperature.

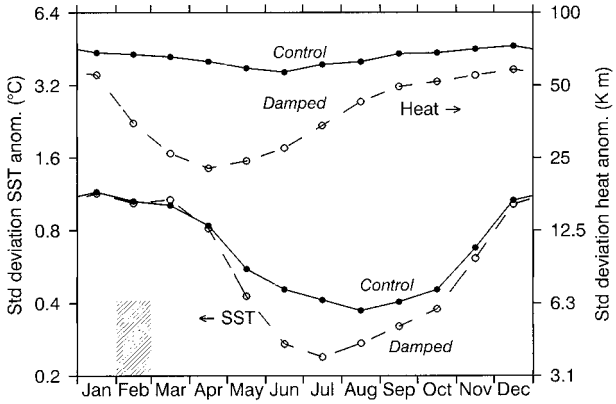

FIG. 8. Standard deviation of model SST and heat anomalies vs time of year for the control run and a damped run (see text). The shaded area indicates the month during which the damping was applied.

- A set of perturbed simulations was carried out in which mixed layer temperature perturbations in spring were generated by changes in the meteorological data and the simulations were continued through the following winter.
- The control run and perturbed simulations were repeated with a model in which temperature perturbations below the mixed layer were strongly damped in summer.

b. Perturbed simulations

In the perturbed simulations the air temperature was increased (in one set of simulations) or decreased (in another) by 1°C for four months ending 30 November; the air temperature perturbation was then removed and each simulation was continued to the end of the following year. The duration of the perturbation was adjusted to generate a subsurface signal matching the pattern exposed by the regression analysis in Fig. 6 that is, with a depth scale—to the 0.6 contour—of around 60 m. The SST response is essentially linear in that there was only a weak asymmetry between the responses to positive and negative perturbations. One-month averages were calculated of the mean difference between the positively and negatively perturbed simulations, and the results were normalized by the mean SST difference for November. The results are presented in Fig. 7, showing SST and subsurface temperatures. The temperature anomaly persists under the mixed layer over summer and autumn and reappears at the surface in the following winter. However, the magnitude of the SST perturbation in winter is only 0.22, approximately one half the magnitude of the spring–winter recurrence effect detected by the regression analysis.

c. Damping of subsurface temperature anomalies

In the damped simulations, temperature perturbations below the mixed layer were strongly damped every summer: the relaxation coefficient γ (section 2a) was increased to 0.2 d^{-1} each February at and below grid cell 8, which is centered at 36 m. This was intended to eliminate persistence of temperature anomalies from the previous spring and winter without immediately affecting the surface. When the perturbed simulations were repeated with damping, spring–winter persistence of the perturbations is effectively eliminated, as expected. For the unperturbed simulation, the effect of damping on the magnitude of heat and SST anomalies is shown in Fig. 8. The standard deviation of heat anomalies drops sharply every year in February; the standard deviation of SST anomalies is not immediately affected but drops three months later in May. In July, the damping reduced the SST variability 40% relative to the undamped simulations, but in summer it has no effect.

When the regression of anomalies against SST in November is repeated and compared with the undamped run (Fig. 9) it is seen that the damping reduces the slope coefficient at 7–10 month lag to 0.3, a reduction of 0.15–0.25; the slope coefficient at these lags still exceeds zero by twice the standard error, so there is still a spring–winter recurrence effect. This is not maintained by subsurface heat storage in the model, so it must be imposed by the atmospheric forcing. The subsurface damping does not affect the regression coefficients in summer (either in the summer immediately following the base month or in the summer after that), which implies that these correlations are not maintained by heat storage at or below the level at which damping is applied.

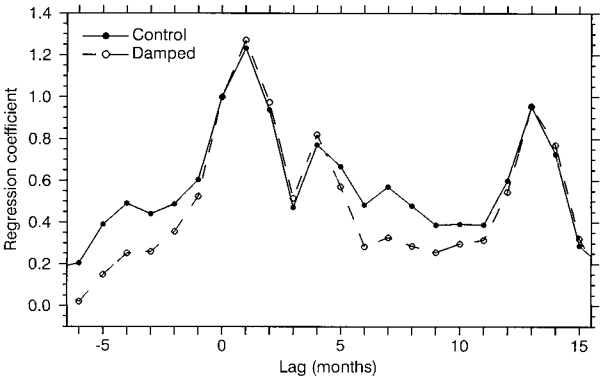

FIG. 9. Slope coefficients from linear regression of SST anomaly in Nov (independent variable) with lagged SST anomaly, for the control run and a damped run.

6. Discussion

The water column model, driven by observed meteorological data, generates a generally good hindcast of observed SST. Agreement is very good in summer when model SST anomalies are highly correlated with observed SST anomalies (r up to 0.95), they are very similar in magnitude and phase, and the simulated anomalies have a slightly longer decorrelation timescale than the observed ones.

Although correlations between simulated and observed SST anomalies remain reasonably high ($r > 0.75$) throughout the year, there are a couple of conspicuous features in the simulated SST that are not so clearly defined in the observed SST. The model exaggerates the seasonal variation in the standard deviation of SST anomalies, and there is a pronounced drop in this quantity in the model between April and June. There is also a break in persistence at around June in the model SST, more pronounced than in observed SST. These features do not appear to correspond to features in the atmospheric forcing. I hypothesize that they are related to the annual breakdown in the seasonal thermocline, and entrainment of water from below. The differences between simulated and observed SST statistics suggest that the temperature of the water below the seasonal thermocline is more variable than represented in the model. This is not surprising, as subsurface temperature variability will be generated by oceanographic processes that are not represented. There is not a lot of data on nonseasonal, subsurface temperature variability in the study area, but Hadfield and Sharples (1996, Fig. 4) show a collection of 117 CTD profiles measured on research voyages distributed irregularly through 14 years. The standard deviation in temperature between soundings below the mixed layer is approximately 0.5°C. If much of this variability is retained in monthly anomalies, then it is possibly large enough to account for missing variance in the simulated SST.

At this site there is a high autocorrelation ($r \sim 0.7$) between SST anomalies in spring and the following winter and a lower correlation with the intervening months. This recurrence of SST anomalies has been attributed elsewhere to the reemergence of subsurface temperature anomalies, stored in and below the seasonal thermocline and reappearing in early winter (Namias and Born 1970, 1974; Alexander and Deser 1995; Alexander and Penland 1996; Bhatt et al. 1998). An examination of subsurface temperature anomalies in the model supports this explanation. A simulation in which an SST anomaly in spring is generated by perturbing the air temperature also shows a reemergence of heat stored below the summer mixed layer but the magnitude of the effect is about half as large as estimated by a linear regression analysis. When heat storage below the summer mixed layer is artificially suppressed, SST variability in the early winter is reduced markedly. This supports the contention that the reduction in SST variability that normally occurs in the model at this time of year is related to entrainment of low-variability deeper water. The artificial suppression of heat storage below the mixed layer reduces the magnitude of the spring–winter recurrence by about one half but does not eliminate it. All these results suggest that *in this model* about half of the spring–winter recurrence is maintained by subsurface processes and half by persistence in the meteorological data.

Because these simulations use fixed meteorological data, they cannot be used to assess the role of feedback of SST on the atmosphere. It may well be that persistence in the near-surface meteorological data is generated locally by the SST anomalies, but it may also involve larger-scale climatic processes.

This study confirms the importance of the seasonal variation in mixed layer depth, which leads to a large variation in the timescale of the ocean's response to atmospheric forcing and causes the deeper ocean to be reexposed to the atmosphere (and vice versa) every year in early winter (at this site, in June). It also highlights the need for better information about subsurface variability in the top few hundred meters of the ocean.

Acknowledgments. This research was carried under FRST Contract CO1628. Thanks to A. Laing, B. Mullan, and anonymous reviewers for helpful comments.

REFERENCES

Alexander, M., and C. Deser, 1995: A mechanism for the recurrence of wintertime midlatitude SST anomalies. *J. Phys. Oceanogr.*, **25,** 122–137.

——, and C. Penland, 1996: Variability in a mixed layer ocean model driven by stochastic atmospheric forcing. *J. Climate,* **9,** 2424–2442.

Ayotte, K. A., and Coauthors, 1996: An evaluation of neutral and convective planetary boundary-layer parameterizations relative to large eddy simulations. *Bound.-Layer Meteor.*, **79,** 131–175.

Berliand, M. E., and T. G. Berliand, 1952: Measurement of the effective radiation of the earth with varying cloud amounts (in Russian). *Izv. Akad. Nauk SSSR Ser. Geofiz.,* **1.**

Bhatt, U., M. Alexander, D. Battisti, D. Houghton, and L. Keller,

1998: Atmosphere–ocean interaction in the North Atlantic: Near-surface variability. *J. Climate,* **11,** 1615–1632.

Bougeault, P., and P. Lacarrere, 1989: Parameterization of orography-induced turbulence in a mesobeta-scale model. *Mon. Wea. Rev.,* **117,** 1872–1890.

Cahill, M. L., J. H. Middleton, and B. R. Stanton, 1991: Coastal-trapped waves on the west coast of South Island, New Zealand. *J. Phys. Oceanogr.,* **21,** 541–557.

Frankignoul, C., 1985: Sea surface temperature anomalies, planetary waves, and air–sea feedback in the middle latitudes. *Rev. Geophys.,* **23,** 357–390.

——, A. Czaja, and B. L'Heveder, 1998: Air–sea feedback in the North Atlantic and surface boundary conditions for ocean models. *J. Climate,* **11,** 2310–2324.

Fung, I. Y., D. E. Harrison, and A. A. Lacis, 1984: On the variability of the net longwave radiation at the ocean surface. *Rev. Geophys. Space Phys.,* **22,** 177–193.

Gaspar, P., Y. Gregoris, and J.-M. Lefevre, 1990: A simple eddy kinetic energy model for simulations of the oceanic vertical mixing: Tests at station Papa and long-term upper ocean study site. *J. Geophys. Res.,* **95,** 16 179–16 193.

Hadfield, M. G., 1995: A meteorological dataset over the sea off the west coast, South Island. New Zealand Oceanographic Institute Physics Section Rep. 1996/3, 10pp. [Available from NIWA, P.O. Box 14-901, Kilbirnie, Wellington, New Zealand.]

——, and J. Sharples, 1996: Modelling mixed layer depth and plankton biomass off the west coast of the South Island, New Zealand. *J. Mar. Syst.,* **8,** 1–29.

Hamilton, L., 1992: Surface circulation in the Tasman and Coral Seas: Climatological features derived from bathy-thermograph data. *Aust. J. Mar. Freshwater Res.,* **43,** 793–822.

Hastenrath, S., and P. J. Lamb, 1978: *Heat Budget Atlas of the Tropical Atlantic and Eastern Pacific Oceans.* The University of Wisconsin Press, 90 pp.

Heath, R. A., 1981: Oceanic fronts around southern New Zealand. *Deep-Sea Res.,* **28A,** 547–560.

——, 1985: A review of the physical oceanography of the seas around New Zealand—1982. *N. Z. J. Mar. Freshwater Res.,* **19,** 79–124.

——, and N. M. Ridgway, 1985: Variability of the oceanic temperature and salinity fields on the West Coast continental shelf, South Island, New Zealand. *N. Z. J. Mar. Freshwater Res.,* **19,** 227–231.

Kalnay, E., and Coauthors, 1996: The NCEP/NCAR 40-year reanalysis Project. *Bull. Amer. Meteor. Soc.,* **77,** 437–471.

Large, W. G., J. C. McWilliams, and S. C. Doney, 1994: Oceanic vertical mixing: A review and a model with a nonlocal boundary layer parameterization. *Rev. Geophys.,* **32,** 363–403.

Levitus, S., M. E. Conkright, R. D. Gelfeld, and T. Boyer, 1994: *World Ocean Atlas 1994* presents new ocean climatologies. *Earth Syst. Monitor,* **5,** 1–2, 13–14.

Moore, M. I., and R. C. Murdoch, 1993: Physical and biological observations of coastal squirts under nonupwelling conditions. *J. Geophys. Res.,* **98,** 20 043–20 061.

Mullan, A., 1998: Southern Hemisphere sea surface temperatures and their contemporary and lag association with New Zealand temperature and precipitation. *Int. J. Climatol.,* **18,** 817–840.

Namias, J., and R. Born, 1970: Temporal coherence in North Pacific sea-surface temperature patterns. *J. Geophys. Res.,* **75,** 5952–5955.

——, and ——, 1974: Further studies of temporal coherence in North Pacific sea surface temperatures. *J. Geophys. Res.,* **79,** 797–798.

Noh, Y., 1996: Dynamics of diurnal thermocline formation in the oceanic mixed layer. *J. Phys. Oceanogr.,* **26,** 2183–2195.

Rahmstorf, S., 1992: Modelling ocean temperatures and mixed-layer depths in the Tasman Sea off the South Island, New Zealand. *N. Z. J. Mar. Freshwater Res.,* **26,** 37–51.

Reynolds, R. W., and T. S. Smith, 1994: Improved global sea surface temperature analyses using optimum interpolation. *J. Climate,* **7,** 929–948.

Smith, S. D., 1988: Coefficients for sea surface wind stress, heat flux, and wind profiles as a function of wind speed and temperature. *J. Geophys. Res.,* **93,** 15 467–15 472.

Stanton, B. R., 1976: Circulation and hydrology off the west coast of the South Island, New Zealand. *N. Z. J. Mar. Freshwater Res.,* **10,** 445–467.

——, 1998: Ocean surface winds off the west coast of New Zealand: A comparison of ocean bouy, ECMWF model, and land-based data. *J. Atmos. Oceanic Technol.,* **15,** 1164–1170.

——, and N. M. Ridgway, 1988: An oceanographic survey of the subtropical convergence zone in the Tasman Sea. *N. Z. J. Mar. Freshwater Res.,* **22,** 583–593.

——, and M. J. Greig, 1991: Hindcasting currents on the west coast shelf of South Island, New Zealand. *Proc. 10th Australasian Conf. on Coastal and Ocean Engineering,* Auckland, New Zealand, Water Quality Centre, 523–527.

——, and M. I. Moore, 1992: Hydrographic observations during the Tasman Boundary Experiment off the west coast of the South Island, New Zealand. *N. Z. J. Mar. Freshwater Res.,* **26,** 339–358.